nature materials

LETTERS

PUBLISHED ONLINE: 6 DECEMBER 2009 | DOI: 10.1038/NMAT2595

A silicon-based electrical source of surface plasmon polaritons

R. J. Walters[1]*, R. V. A. van Loon[1], I. Brunets[2], J. Schmitz[2] and A. Polman[1]

After decades of process scaling driven by Moore's law, the silicon microelectronics world is now defined by length scales that are many times smaller than the dimensions of typical micro-optical components. This size mismatch poses an important challenge for those working to integrate photonics with complementary metal oxide semiconductor (CMOS) electronics technology. One promising solution is to fabricate optical systems at metal/dielectric interfaces, where electromagnetic modes called surface plasmon polaritons (SPPs) offer unique opportunities to confine and control light at length scales below 100 nm (refs 1, 2). Research groups working in the rapidly developing field of plasmonics have now demonstrated many passive components[3,4] that suggest the potential of SPPs for applications in sensing[5] and optical communication[6]. Recently, active plasmonic devices based on III–V materials[7–9] and organic materials[10] have been reported. An electrical source of SPPs was recently demonstrated using organic semiconductors by Koller and colleagues[11]. Here we show that a silicon-based electrical source for SPPs can be fabricated using established low-temperature microtechnology processes that are compatible with back-end CMOS technology.

Depending on geometry and wavelength, an SPP can propagate with an effective wavelength that is much smaller than the free-space wavelength of photons at the same frequency. Owing to this difference, light cannot directly couple into SPP modes. In a typical plasmonics experiment, a prism or grating is used to overcome the wavelength mismatch and allows SPPs to be launched by an external laser source. However, optical excitation is impractical for many imagined future applications, especially those in chemical or biological sensing where minimum cost and maximum parallel functionality will be beneficial or requisite. The development of electrically excited SPP sources is therefore of critical importance for future integrated plasmonic device technology.

The metal–insulator–metal (MIM) plasmon waveguide geometry[12,13] is particularly promising for electrically driven SPP sources, because the metallic cladding layers that support and guide the SPP mode can also serve as contact electrodes. MIM waveguide SPP modes are highly confined within the insulating region[14]. In our devices, optically thick gold cladding layers surround a semi-insulating layer of alumina that contains silicon quantum dots. When a sufficient voltage is applied across the insulator layer, tunnelling electrons excite the embedded quantum dots by impact ionization processes. As the insulator layer of this MIM waveguide is too thin to support photonic modes, the excited quantum dots decay radiatively only by direct near-field coupling to plasmonic modes[15]. This results in the electrically driven excitation of SPPs over a spectral range determined by the properties of the silicon quantum dots.

Typically, silicon nanocrystals are created in a silica host material by annealing silicon-rich silicon oxides (SiO_x; $x < 2$) at high temperatures (>900 °C; ref. 16). These methods are incompatible with the maximum temperatures that can be tolerated during back-end CMOS processing without damaging the underlying metal interconnect layers (~425 °C; ref. 17). In our fabrication process, the optically active silicon nanocrystal material is instead obtained by sequential atomic layer deposition (ALD) of Al_2O_3 (at 300 °C) and low-pressure chemical vapour deposition (LPCVD) of silicon nanocrystals (at 325 °C; ref. 18). Five layers of alumina and four interstitial layers of nanocrystals were grown without a vacuum break for a total insulator layer thickness of 100 nm. We fabricated suspended membrane MIM structures incorporating this active material between two 200-nm-thick gold cladding layers. This geometry allows electrical and optical access to both interfaces of the MIM waveguide. Arrays of devices consisting of paired out-coupling grating structures and electrical isolation trenches were then created in the cladding layers using focused ion beam (FIB) milling. A schematic representation of our device and images recorded with a scanning electron microscope (SEM) are shown in Fig. 1.

The optical properties of silicon nanocrystals have been extensively studied[16]. Near-infrared luminescence is associated with radiative exciton decay across the quantum-confined bandgap and at oxygen-related interface trap sites[19,20]. The emission spectrum is typically inhomogeneously broadened over several hundred nanometres owing to the distribution of nanocrystal diameters, but the output wavelength can in principle be tuned over this wide range by selecting only nanocrystals of an appropriate size[21]. Figure 2a shows an image of a single silicon nanocrystal in alumina recorded with a transmission electron microscope (inset), together with a representative photoluminescence spectrum for a sample excited by the 488 nm line of an Ar^+ ion laser at low power (10^{17} photons s^{-1} cm^{-2}). By comparing the photoluminescence properties to a reference sample containing silicon nanocrystals in silica[22], we estimate the internal radiative quantum efficiency of the silicon nanocrystals in our doped-alumina material is ~1%. This low value is attributed to poor surface passivation of the silicon nanocrystals in alumina, which may be improved by optimizing the deposition conditions.

Efficient electrical excitation of silicon nanocrystals is challenging owing to the insulating matrix that must necessarily surround the nanocrystals to provide the carrier confinement[23,24]. In our device, we generate excitons by hot-carrier impact ionization when a current flows through the insulating alumina host containing the nanocrystals at moderate voltages (10–20 V). We measured the electroluminescence spectrum of the silicon nanocrystals embedded in Al_2O_3 in metal–insulator–semiconductor (MIS) diode structures made by sputtering a thin (20 nm) gold electrode

[1]Center for Nanophotonics, FOM Institute for Atomic and Molecular Physics, Science Park 113, 1098 XG Amsterdam, The Netherlands, [2]MESA+ Institute for Nanotechnology, University of Twente, PO Box 217, 7500 AE Enschede, The Netherlands. *e-mail: walters@amolf.nl.

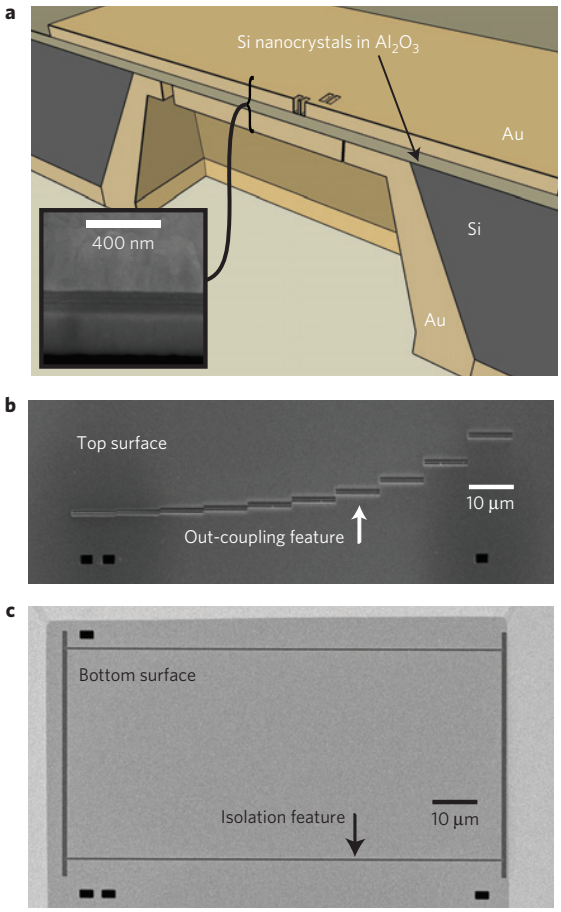

Figure 1 | Schematic of the device and SEM images. a, A schematic of a device in cross-section (not to scale), with a high-magnification SEM image of the MIM waveguide cross-section (inset). Individual Si nanocrystals embedded between the two metal cladding layers are too small to resolve, but some contrast with the surrounding Al_2O_3 layers is evident. **b**,**c**, SEM images of the top (**b**) and bottom (**c**, mirrored) surfaces of a membrane after FIB patterning. Out-coupling structures are visible in the top surface, each at a different distance from the electrical isolation groove milled by FIB in the bottom surface.

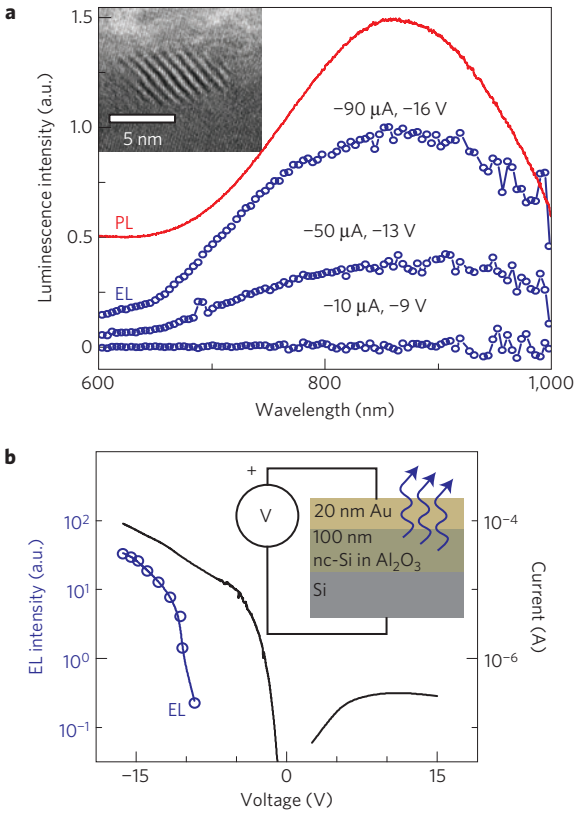

Figure 2 | Electroluminescence properties of Si nanocrystals in Al_2O_3. **a**, Si nanocrystals in alumina emit near-infrared light from an MIS diode test structure. The electroluminescence (EL) spectra are similar to a typical photoluminescence (PL) spectrum (shown offset by 0.5) when corrected for electrode transmission. A single embedded nanocrystal can be seen in a plan-view transmission electron microscope image (inset) as a region of Moiré fringes against the underlying single-crystal silicon substrate. **b**, The *I*–*V* characteristics of the test structure (inset) show the rectifying effect of the MIS diode at positive voltages. At negative applied bias, the integrated electroluminescence intensity rises in proportion to the current magnitude, consistent with excitation by impact ionization.

over the active insulator layer on a silicon substrate. The electroluminescence spectra strongly resemble the photoluminescence spectra after correcting for the transmission spectrum of the contact electrode (Fig. 2a).

The current–voltage (I–V) characteristics of the test structure (schematic shown in the inset of Fig. 2b) are consistent with the behaviour expected for an MIS diode[25]. In the forward bias condition, the applied negative voltage falls primarily across the substrate body diode, whereas under reverse bias conditions, there is a larger potential drop across the insulator layer and a reduced total current. We observe electroluminescence when the applied reverse bias is below −10 V (or above +35 V). The integrated intensity of the electroluminescence spectrum, shown in Fig. 2b, grows in proportion to the current flowing through the device, and no electroluminescence is observed from control devices that do not contain silicon nanocrystals. We estimate that the external power efficiency for electroluminescence in this particular device is $<10^{-6}$. Further optimization of the device structure could improve the efficiency by several orders of magnitude[24], but this is not the focus of this letter.

Nanocrystals in our MIM membrane devices are similarly excited by impact ionization when a current flows through the structure. In these devices, the metallic cladding layers are optically thick and the exciton recombination energy from excited silicon nanocrystals is coupled to SPP waveguide modes. The mode structure for a two-dimensional MIM waveguide can be calculated numerically using dielectric constant values determined by variable-angle spectral ellipsometry[26]. We find that an MIM waveguide with a nanocrystal-doped Al_2O_3 layer less than ∼150 nm thick supports only one propagating SPP mode. This plasmonic mode is characterized by a magnetic field with a normal component (H_y) that is symmetric across the centre of the waveguide. The mode has a propagation length that depends on the insulator layer thickness. In our fabrication process, we targeted an insulator thickness of 100 nm to balance the electrical performance of the device with the SPP propagation length (∼3–5 μm) over the emission range of the Si nanocrystals (600–900 nm). The locations of the nanocrystal layers within the waveguide must be controlled to ensure good coupling between the nanocrystals and the desired SPP mode. Calculations show the nanocrystals should be separated from the metallic cladding layers by at least 10 nm to avoid strong quenching by coupling to so-called lossy surface waves and that the centre of the insulating layer is the preferred location for maximum coupling to the symmetric-H_y mode[27,28]. Further details of the coupling model are given in the Supplementary Information.

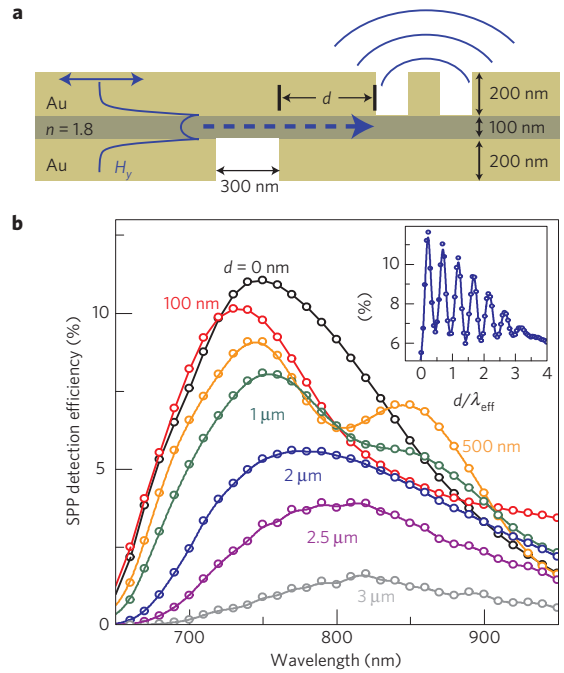

Figure 3 | Simulated SPP detection efficiency. a, A schematic of the two-dimensional geometry used to approximate the devices in finite-difference time-domain simulations. **b**, The simulated spectral-detection efficiency decreases and redshifts as the distance d between the isolation slit and the out-coupling structure increases. Note the characteristic spectral oscillations that result from Fabry–Perot resonances within the passive MIM waveguide section, shown as an inset for a free-space wavelength of 800 nm ($\lambda_{eff} = 350$ nm).

We used finite-difference time-domain simulations to study the expected far-field detection efficiency for SPPs generated in the active area of the device using a two-dimensional approximation of our device geometry (shown schematically in Fig. 3a). Further details of these calculations are described in the Supplementary Information. The calculated power transfer to the far-field is shown in Fig. 3b, normalized to twice the launched power at each wavelength to model coupling to SPPs that propagate in both directions. We find that up to 10% of the power coupled from nanocrystals into SPPs can be scattered out by the out-coupling structure. As the distance between the isolation feature and the out-coupling structure (d) is increased, we expect the scattered SPP signal to decay according to the calculated $1/e$ propagation length at each wavelength. Shorter propagation lengths at shorter wavelengths cause an overall redshift of the spectrum with increasing d. Calculations also predict characteristic spectral oscillations in throughput when the distance from the isolation trench to the out-coupling feature is less than ~1 μm. These oscillations result from the interplay of Fabry–Perot resonances within the passive section of the waveguide and SPP dispersion. Importantly, these characteristic spectral oscillations can confirm the excitation of SPPs on the basis of emission spectra measured for individual devices.

The electrical characteristics of the MIM device resemble the I–V curve shown in Fig. 2 because a parasitic MIS diode in parallel with the MIM capacitor dominates the circuit impedance. When a bias below −10 V (or above +10 V) is applied to our MIM device, we observe light at locations where we have created out-coupling structures in the top cladding layer (Fig. 4a,b). The polarization state of the detected light (Fig. 4c) is oriented perpendicular to the out-coupling structure as expected for light emitted from a narrow slit. We attribute this emission to the scattering of SPPs that have propagated through the passive MIM waveguide section to the out-coupling structures from the active region of the device. Light propagating through the waveguide must be attributed to SPPs because the device structure supports only the symmetric-H_y SPP mode. The possibility that light is also generated at the edge of the out-coupling structure, where nanocrystals might couple directly to radiative modes, is mitigated by the electrical isolation trench in the bottom surface of the membrane. In addition, Fig. 4d

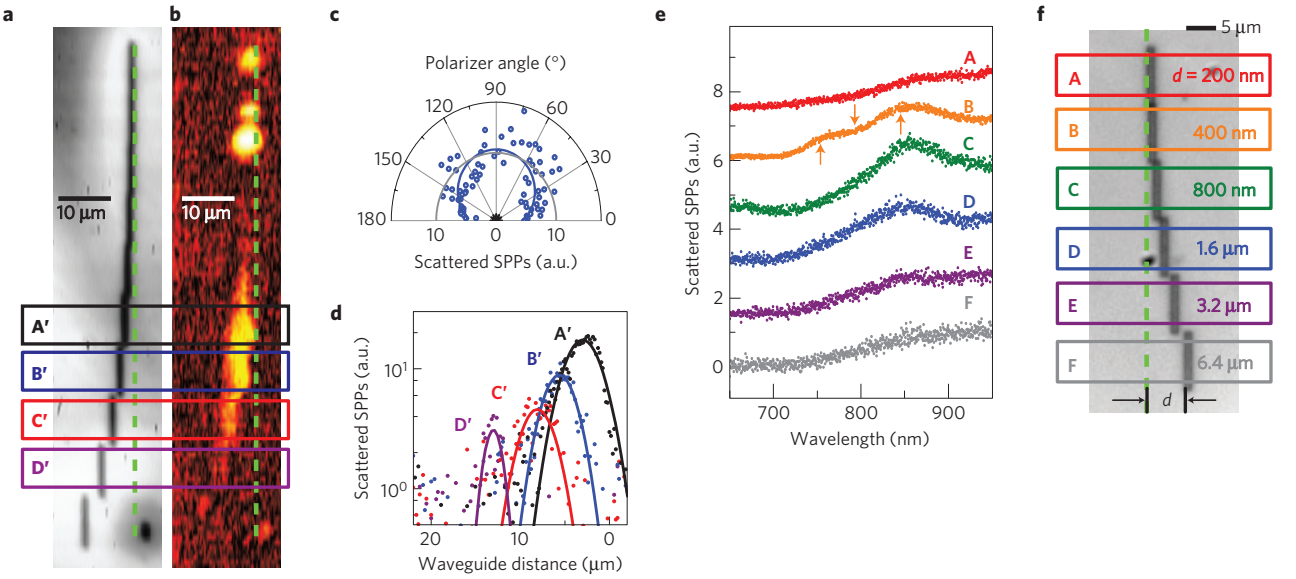

Figure 4 | Electrical generation of SPPs. a,**b**, A membrane containing ten devices (**a**) emits light (**b**) from scattered SPPs at the locations of the out-coupling structures ($V = -16.8$ V, $I = -1.2$ mA). The location of the isolation slit on the bottom surface of the membrane is indicated by the green dashed line. **c**, The light is found to be polarized perpendicular to the out-coupling structures. **d**, The intensity variation of the signal reveals that the SPP source efficiency is not uniform over the scale of the membrane (~50 μm), but some regions show the anticipated SPP intensity decay behaviour. **e**,**f**, Oscillations corresponding to Fabry–Perot resonances within the passive MIM waveguide segment are clearly observed in the normalized spectra (**e**) measured for devices on another membrane (**f**), confirming the excitation of SPPs ($V = -15.4$ V, $I = -1.1$ mA).

shows a membrane region in which the integrated signal intensity drops exponentially in magnitude with distance over four adjacent devices (Fig. 4a: A′–D′). The best-fit decay constant is $4.4 \pm 0.6\,\mu m$, which closely matches the calculated average decay length over the emission range of the silicon nanocrystals (4.5 μm). A further plot of the peak intensity data from this measurement can be found in the Supplementary Information.

Owing to non-uniformity in the electrically pumped active region, the emission intensity varies between devices fabricated on a single membrane. This requires us to rely on spectral measurements to unambiguously confirm the propagation of SPPs in the MIM waveguide. Direct evidence for the electrical generation of SPPs in our devices can be seen in the characteristic oscillations observed in the emission spectra shown in Fig. 4e. Local maxima near 750 and 850 nm surround a local minimum near 800 nm for a device designed to have a passive MIM waveguide length of 400 nm. These spectral features correspond well to Fabry–Perot resonance-related spectral oscillations in SPP detection efficiency found in Fig. 3b when the simulated passive waveguide separation length is 500 nm. Moreover, the out-scattered SPP spectra generally overlap with the electroluminescence spectra shown in Fig. 2a and show a redshift as the length of the passive MIM waveguide section is increased, as expected. The exact spectrum of light scattered from the SPPs depends on many factors, including the luminescent nanocrystal distribution inside the MIM waveguide, the spectral coupling efficiency between the nanocrystals and the MIM waveguide mode and the distance that SPPs travel within the active waveguide region from the point of generation to the isolation trench.

Although a membrane device offers many advantages for our experiments, it is relatively fragile and therefore unlikely to be useful for practical applications. The primary difficulty in fabricating a robust back-end CMOS-integrated surface-supported device may be the growth of the first alumina insulator layer by ALD on gold. If a suitable process proves to be impossible to develop, we suggest that the gold bottom cladding layer could be replaced with a chemically and mechanically polished aluminium electrode. This change of material will provide a high-quality growth surface for the ALD/LPCVD active insulator layer at the cost of a reduced SPP propagation length. We also note that gold has not historically been considered a CMOS-compatible material, as it diffuses rapidly through silicon. However, in recent years microchips designed to interface with living tissue (bio-chips) have been fabricated with gold top electrodes, as aluminium is poisonous to living cells. This new development has shown that the gold compatibility problem can be overcome[29]. With modest near-term improvements in performance, our design might be usefully incorporated in the optical sensor plane of a bio-chip with an underlying CMOS logic plane. Over the long term, our results may pave the way for future silicon-based plasmonic sources for optical communication.

We have demonstrated that a silicon-based electrically driven source of SPPs can be fabricated at low temperatures using an MIM waveguide geometry. Our experiments suggest a new route forward towards high-density, active plasmonic circuits that are integrated with silicon microelectronics.

Methods

Using ALD, 20 nm of alumina was deposited onto a clean p-type (5–10 Ω cm) Si substrate in 245 ALD cycles of water and trimethylaluminium at a substrate temperature of 300 °C. Without breaking the vacuum, the wafer was transferred to a LPCVD reactor, where Si was deposited using Si_3H_8 as the precursor gas. The LPCVD process temperature was 325 °C. Prolate silicon nanocrystals with a minor diameter of ~3 nm form *in situ* with a typical single-layer areal density of $2 \times 10^{12}\ cm^{-2}$ during a deposition period of 10 min. This procedure was repeated four times, to grow four monolayers of Si nanocrystals encapsulated in five 20-nm-thick Al_2O_3 layers for a total insulator layer thickness of 100 nm (ref. 18).

After deposition of the active material, 200 nm of gold was sputtered onto the sample to form the top gold cladding/contact layer. On the reverse side of the wafer, 300 nm of SiO_2 was then deposited by plasma-enhanced chemical vapour deposition, patterned using optical lithography and etched in buffered hydrofluoric acid solution to serve as a hard mask for a tetramethyl ammonium hydroxide anisotropic etch solution[30]. The wafer was back-etched to the alumina layer to create membranes of $50 \times 100\,\mu m$ and attached with photoresist to a Pyrex carrier wafer for mechanical stability during further processing. The top gold layer was patterned using optical lithography with contact pads (2×1 mm) aligned to the membranes etched from the reverse wafer surface. After separating the dies, a gold etchant (KI) was used to transfer the pattern to the top gold layer. The bottom cladding/contact layer was then formed by sputtering 200 nm of gold to the bottom side of the die through a physical mask.

With an FIB system, alignment marks through the entire membrane and 240-nm-wide isolation trenches through the bottom gold layer were milled to create an electrically isolated region. After this, the sample was turned over so that further structures could be made on the top surface. Out-coupling features designed to scatter SPPs into the far-field were milled in alignment with the electrically isolated region in the bottom side. The out-coupling structures consist of two 270-nm-wide slits in the top gold cladding layer, separated by a 70-nm-wide bar of gold.

During electrical measurements, the membranes were contacted with tungsten probe needles and driven by a current source to avoid thermal-runaway problems. Scattered light from SPPs was collected through a ×50 (NA = 0.45) (Fig. 4a) or ×100 (NA = 0.73) (Fig. 4e) objective with a long working distance and imaged onto a thermo-electrically cooled CCD (charge-coupled device) camera. Spectra were collected using an imaging grating spectrometer with the sample aligned with the entrance slits to allow simultaneous collection from several out-coupling structures. All spectra are filtered to remove spikes from cosmic rays and corrected for the shift introduced by the real-space offset of each structure within the image at the spectrometer entrance slits.

Received 10 August 2009; accepted 5 November 2009; published online 6 December 2009

References

1. Raether, H. *Surface Plasmons on Smooth and Rough Surfaces and on Gratings* (Springer Tracts in Modern Physics, Vol. 111, Springer, 1988).
2. Barnes, W. L., Dereux, A. & Ebbesen, T. W. Surface plasmon subwavelength optics. *Nature* **424,** 824–830 (2003).
3. Bozhevolnyi, S. I., Volkov, V. S., Devaux, E., Laluet, J.-Y. & Ebbesen, T. W. Channel plasmon subwavelength waveguide components including interferometers and ring resonators. *Nature* **440,** 508–511 (2006).
4. Ebbesen, T. W., Genet, C. & Bozhevolnyi, S. I. Surface-plasmon circuitry. *Phys. Today* **61,** 44–50 (2008).
5. Homola, J. (ed.) in *Surface Plasmon Resonance Based Sensors* (Springer Series on Chemical Sensors and Biosensors, Vol. 4, Springer, 2006).
6. Ozbay, E. Plasmonics: Merging photonics and electronics at nanoscale dimensions. *Science* **311,** 189–193 (2006).
7. Neutens, P., van Dorpe, P., De Vlaminck, I., Lagae, L. & Borghs, G. Electrical detection of confined gap plasmons in metal–insulator–metal waveguides. *Nature Photon.* **3,** 283–286 (2009).
8. Hill, M. T. *et al.* Lasing in metallic-coated nanocavities. *Nature Photon.* **1,** 589–594 (2007).
9. Hill, M. T. *et al.* Lasing in metal–insulator–metal sub-wavelength plasmonic waveguides. *Opt. Express* **17,** 11107–11112 (2009).
10. Yates, C. J., Samuel, D. W., Burn, P. L., Wedge, S. & Barnes, W. L. Surface plasmon-polariton mediated emission from phosphorescent dendrimer light-emitting diodes. *Appl. Phys. Lett.* **88,** 161105 (2006).
11. Koller, D. M. *et al.* Organic plasmon-emitting diode. *Nature Photon.* **2,** 684–687 (2008).
12. Economou, E. N. Surface plasmons in thin films. *Phys. Rev.* **182,** 539–554 (1969).
13. Verhagen, E., Dionne, J. A., Kuipers, L., Atwater, H. A. & Polman, A. Near-field visualization of strongly confined surface plasmon polaritons in metal–insulator–metal waveguides. *Nano Lett.* **8,** 2925–2929 (2008).
14. Miyazaki, H. T. & Kurokawa, Y. Squeezing visible light waves into a 3-nm-thick and 55-nm-long plasmon cavity. *Phys. Rev. Lett.* **97,** 097401 (2006).
15. Jun, Y. C., Kekatpure, R. D., White, J. S. & Brongersma, M. L. Nonresonant enhancement of spontaneous emission in metal–dielectric–metal plasmon waveguide structures. *Phys. Rev. B* **78,** 153111 (2008).
16. Pavesi, L. & Lockwood, D. J. (eds) in *Silicon Photonics* (Topics in Applied Physics Series, Vol. 94, Springer, 2004).
17. Schmitz, J. Adding functionality to microchips by wafer post-processing. *Nucl. Instrum. Methods* **576,** 142–149 (2007).
18. Brunets, I. *et al.* Low-temperature LPCVD of Si nanocrystals from disilane and trisilane (Silcore) embedded in ALD-alumina for non-volatile memory devices. *Surf. Coat. Technol.* **201,** 9209–9214 (2007).
19. Godefroo, S. *et al.* Classification and control of the origin of photoluminescence from Si nanocrystals. *Nature Nanotech.* **3,** 174–178 (2008).

20. Hadjisavvas, G. & Kelires, P. C. Structure and energetics of Si nanocrystals embedded in a-SiO_2. *Phys. Rev. Lett.* **93,** 226104 (2004).
21. Brongersma, M. L., Polman, A., Min, K. S., Tambo, T. & Atwater, H. A. Tuning the emission wavelength of Si nanocrystals in SiO_2 by oxidation. *Appl. Phys. Lett.* **72,** 2577–2579 (1998).
22. Walters, R. J., Kalkman, J., Polman, A., Atwater, H. A. & de Dood, M. J. A. Photoluminescence quantum efficiency of dense silicon nanocrystal ensembles in SiO_2. *Phys. Rev. B* **73,** 132302 (2006).
23. Irrera, A. *et al.* Electroluminescence properties of light emitting devices based on silicon nanocrystals. *Physica E* **16,** 395–399 (2003).
24. Marconi, A. *et al.* High power efficiency in Si-nc/SiO_2 multilayer light emitting devices by bipolar direct tunnelling. *Appl. Phys. Lett.* **94,** 221110 (2009).
25. Sze, S. M. *Physics of Semiconductor Devices* 2nd edn (Wiley, 1981).
26. Dionne, J. A., Sweatlock, L. A., Atwater, H. A. & Polman, A. Plasmon slot waveguides: Towards chip-scale propagation with subwavelength-scale localization. *Phys. Rev. B* **73,** 035407 (2006).
27. Ford, G. W. & Weber, W. H. Electromagnetic interactions of molecules with metal surfaces. *Phys. Rep.* **113,** 195–287 (1984).
28. Hryciw, A. C., Jun, Y. C. & Brongersma, M. L. Plasmon-enhanced emission from optically-doped MOS light sources. *Opt. Express* **17,** 185–192 (2008).
29. Benini, L., Guiducci, C. & Paulus, C. Electronic detection of DNA hybridization: Toward fully-electronic microarrays. *IEEE Des. Test Comput.* **24,** 38–48 (2007).
30. Yan, G. *et al.* An improved TMAH Si-etching solution without attacking exposed aluminium. *Sensor Actuat. A* **89,** 135–141 (2001).

Acknowledgements

This work is part of the research programme of the FOM and was financially supported by NWO. It was also supported by the NanoNed technology programme and the Smart Mix Programme of the Netherlands Ministry of Economic Affairs and the Dutch Technology Foundation STW.

Author contributions

I.B. prepared samples through the membrane-etch process under the supervision of J.S. R.V.A.v.L. and R.J.W. completed the sample fabrication and together carried out the experiments and analysis under the supervision of A.P. The manuscript was prepared by R.J.W. with input from all co-authors.

Additional information

The authors declare no competing financial interests. Supplementary information accompanies this paper on www.nature.com/naturematerials. Reprints and permissions information is available online at http://npg.nature.com/reprintsandpermissions. Correspondence and requests for materials should be addressed to R.J.W.